Effect of Microstructure on Atmospheric-Induced Corrosion of Heat-treated Grade 2205 and 2507 Duplex Stainless Steels

Effect of Microstructure on Atmospheric-Induced Corrosion of Heat-treated Grade 2205 and 2507 Duplex Stainless Steels

Cem Örnek [1,2], *Amina H. Ahmed* [1] *& Dirk L. Engelberg* [1,2]

[1] *Corrosion and Protection Centre,*
[2] *Research Centre for Radwaste and Decommissioning (RCRD)*
School of Materials, The University of Manchester, Oxford Road, M13 9PL, UK

Abstract

Atmospheric-induced corrosion tests under $MgCl_2$ salt deposits were carried out on duplex stainless steel grade 2205 and 2507. As-received and 750°C heat-treated material conditions were investigated, and selected micro-structural sites targeted with salt-laden deposits to determine their corrosion response. Deposits were wetted under controlled climatic conditions at 80°C and 40% relative humidity. Observations of micro-structural attack indicated the presence of net anodic and net cathodic sites. Ferrite was net anode with respect to austenite and hence more susceptible to atmospheric-induced corrosion in both as-received microstructures. Ferrite and ferrite/austenite interfaces were selectively attacked in heat-treated grade 2205, whereas mainly primary and secondary austenite in heat-treated grade 2507. Scanning Kelvin Probe Force Microscopy and Magnetic Force Microscopy were used to obtain high-resolution information about susceptible microstructure sites.

Introduction

Duplex stainless steels (DSS) typically contain a balanced ratio of ferrite (α) to austenite (γ), resulting in synergistic effects on their corrosion resistance and material properties [1]. For example, DSS have higher mechanical strength and show better stress corrosion cracking resistance than most of the common austenitic stainless steel grades. DSS are therefore candidate material for critical applications, including the potential use of grade 2205 as Intermediate Level Radioactive Waste (ILW) containers [2-3]. To ensure long-term structural integrity, it is important to understand the propensity of these materials to localised corrosion and stress corrosion cracking.

Atmospheric-induced corrosion (AIC) and stress corrosion cracking (AISCC) can occur in austenitic stainless steel at temperatures below 50°C [4]. Cases of chloride-induced AISCC have also been reported in DSS at temperatures below 100°C [5]. To predict the behaviour and inform about potentially susceptible crack nucleation sites, the effect of microstructure needs to be fully understood. In terms of micro-structural characterisation, the Scanning Kelvin Probe Force Microscopy (SKPFM) is a powerful tool as it allows local variations in contact potential difference (Volta/Surface potential) to be determined with sub-micron resolution. Volta potential differences have been reported to show under certain circumstances linear correlation with their corresponding corrosion potentials [6-7]; thus SKPFM is a unique technique to estimate local changes in corrosion behaviour with a lateral resolution of ca. 100 nm and a potential sensitivity of 1 mV [8]. The technique also allows determination of the work function of the specimen, if the work function of the analysis tip is known. The

difference in the magnetic behaviour of ferrite and austenite can be determined via Magnetic Force Microscopy (MFM). In the latter technique a magnetised tip is scanned over the surface, and the tip-sample magnetic interactions are used to produce a map of the magnetic response. MFM can be used to reveal the magnetic microstructure, for example small austenitic islands within ferrite and vice versa, with very high spatial resolution, typically less than 50 nm [9].

The work reported in this paper addresses the propensity of as-received and 750°C heat-treated grade 2205 and 2507 duplex stainless steels to atmospheric-induced corrosion (AIC) in chloride-containing environments. Metallographic observations, augmented by SKPFM and MFM measurements have been used to characterise microstructure effects that may impact on long-term material performance. This work is part of a larger project on time-dependent characterisation of corrosion and stress corrosion cracking processes.

Experimental Procedures

Coupon samples of duplex stainless steel grade 2205 and 2507 with dimensions of 15 mm (length) x 10 mm (width) x 5 mm (thickness) were used for this study, with the chemical compositions shown in Tab. 1. Both as-received materials were in a solution annealed material condition. Specimens of both grades were heat treated at 750°C for 3 hours, followed by a water quench. The as-received and heat treated samples were then ground to 4000 grit with SiC paper ($R_a \approx 3$ µm), cleaned with soapy water and acetone. Droplets with volumes of 0.5, 1.5 and 2.5 µl of a 0.1 M aqueous $MgCl_2$ solution were deposited onto the surfaces. The salt deposition density of these droplets was calculated as 210, 350 and 420 µg/cm², respectively. In this work atmospheric corrosion after salt droplet exposure of 420 µg/cm² deposition density will be presented only. Effects of different salt deposition densities, however, will be reported in a separate publication. The salt-laden samples were exposed to controlled climatic conditions at 80°C/40% relative humidity (RH) in a Binder KBF 240 climate chamber. At 80°C the deliquescence point for $MgCl_2$ is at around 26% RH [3]. Under these conditions a less than saturated $MgCl_2$ liquid film is formed on the surface. The exposure time (i.e. the time of wetness) was 7 days. After AIC exposure, the samples were washed with water and cleaned in 10 wt.-% citric acid at 80°C for 2 hours.

A Zeiss Evo 50 Scanning Electron Microscope (SEM), interfaced to an Oxford Inca Energy Dispersive X-ray (EDX) system was used for microstructure analysis. Electrolytic etching in 56 wt.-% KOH and 10 wt.-% Oxalic acid was carried out for microstructure analysis. SKPFM and MFM measurements were carried out on a separate set of specimens polished to ¼ µm diamond finish, and subsequently cleaned with acetone and replicating tape. A Nanoscope Dimension 3100 Atomic Force Microscope was used, with data evaluation carried out using the Nanoscope analysis software version 1.4. Surface potential measurements were performed with Pt coated OSCM-PT (Bruker) probes, and magnetic frequency scans of the same area with MESP-HM (Bruker) probes. The scan range was 80 µm x 80 µm for the as-received material condition, to image large areas of the austenitic and ferritic phases. The 750°C annealed sample was scanned over an area of 40 µm x 40 µm, to reveal higher resolution information about secondary phases. The scan rate was 0.200 Hz and the drive amplitude 5000 mV with a lift height of 100 nm. All SKPFM and MFM investigations were performed in ambient conditions at temperatures of ca. 25°C.

Tab. 1: Chemical composition of grade 2205 and 2507 used in this study (wt.-%)

Grade	C	Si	Mn	P	S	Cr	Ni	Mo	N	W	Cu	Fe
2205	0.016	0.4	1.5	0.021	0.001	22.4	5.8	3.2	0.18	-	-	bal.
2507	0.02	0.4	0.65	0.026	0.002	25.4	7.05	3.7	0.23	0.62	0.63	bal.

Results and Discussion

Metallography and Microstructure

DSS grade 2205 and grade 2507 have similar microstructures in the as-received condition, consisting of a solution annealed microstructure with austenite and ferrite, shown in Fig. 1 (a,c). Fig. 1 (b,d) summarises the heat-treated material conditions of both grades. 2507 has a higher proportion of alloying elements than 2205, and is therefore more prone to precipitate secondary phases after heat treatment [10], noticeable in Fig. 1 (d). Phases were identified based on their chemical compositions by using EDX analysis. Austenite is generally enriched in γ-forming elements (Ni, N), whilst ferrite, sigma and chi phase are enriched in α-formers (Cr, Mo), with the latter two containing higher Cr and Mo contents. Sigma phase is generally more enriched in Cr, whilst chi-phase is more enriched in Mo.

Elemental analysis of heat-treated grade 2205 in Fig. 1 (b) indicates the presence of austenite, surrounded by regions containing ferrite (α) and sigma (σ) and/or chi (χ) phase, with possibly the presence of some secondary austenite (γ'). Isolated Cr- and Mo-rich precipitates (χ or σ) have been identified by EDX analysis, but their exact compositions could not unambiguously be determined and assigned.

Fig. 1 (d) shows the microstructure of heat-treated grade 2507, and Fig. 2 summarises additional EDX line profiles. The brightest regions (α/γ-interface) contain significantly increased Cr (26-30%), Mo (13-18%), and Si (0.9-1.3%) contents, related to χ-phase. The σ-phase in this microstructure has higher Cr (30-33%) contents, with less Mo (4-7%) and Si (0.6-0.7%). Austenitic grains are still apparent, but no ferrite was observed in the region investigated. However, ferrite may have transformed into smaller islands and the presence of remaining ferrite in the microstructure cannot be excluded.

Elemental analysis of the discrete dark regions in both 2205 and 2507 indicate the presence of (Fe,Cr)-based carbides and nitrides. According to Kim et al. [9], carbides of type $M_{23}C_6$ are mainly located at α/γ-phase boundaries, and nitrides of type Cr_2N typically precipitate within the austenitic phase. Hence, most likely both carbides and nitrides are present in our heat-treated microstructures (Fig. 1 and Fig. 2). Further TEM investigations will elucidate the microstructure of those secondary precipitates in detail.

Trasatti et al. [11] reported the presence of 7.9 vol.% σ-phase in a 22% Cr DSS using similar heat treatments. In contrast, Arıkan et al. [12] determined for grade 2205 heat-treated at 725°C for 5 ¼ hrs only the presence of 0.6 vol.% σ-phase. The σ-phase generally precipitates inside grains, at α/α and α/γ grain boundaries, following the eutectoid reaction: ferrite (α) → sigma (σ) + secondary austenite (γ'). Kim et al. [13] showed that χ, σ and γ' were present in the microstructure of a cast DSS alloy

(CD3MN) with a composition of 23.5-24% Cr after 30 days at 850°C. However, χ-phase could not be differentiated from σ-phase in the latter work.

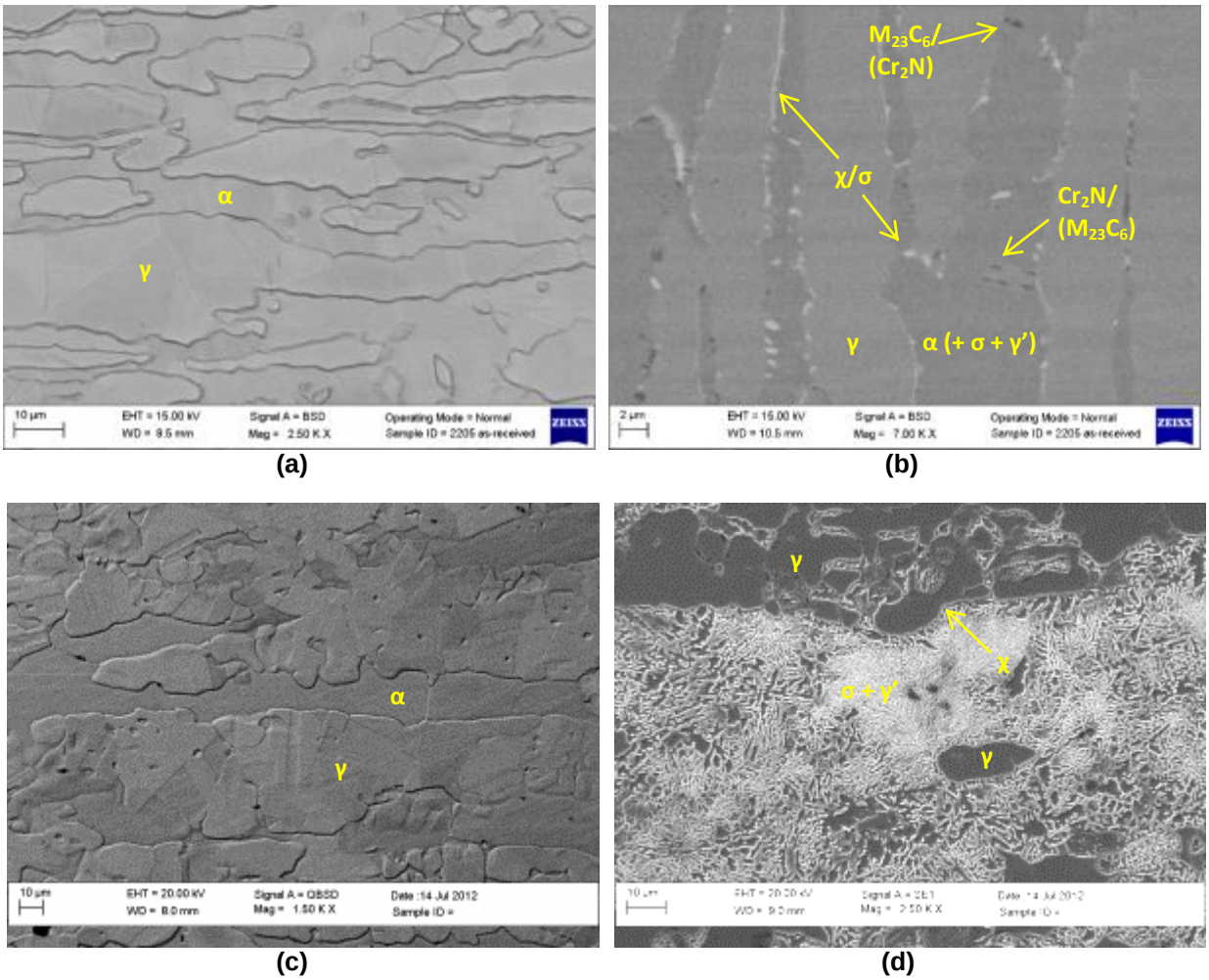

Fig. 1: Backscattered-SEM images showing the microstructure of (a) 2205 as-received (oxalic acid etched), (b) 2205 750°C/3h heat-treated (unetched), (c) 2507 as-received (oxalic acid etched) and (d) 2507 750°C/3h heat-treated conditions (oxalic acid etched).

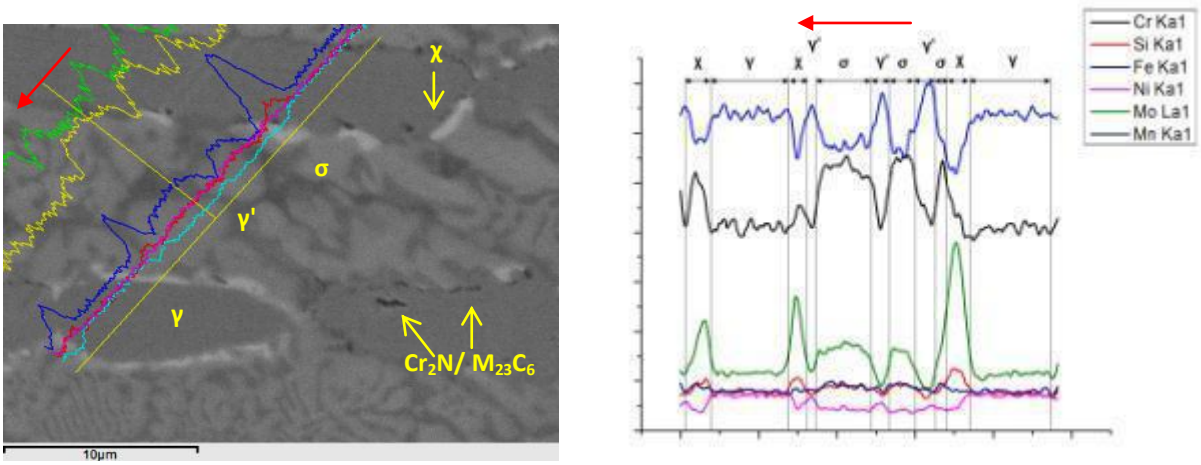

Fig. 2: Backscattered-SEM image with EDX line scans of heat-treated 2507 (750°C/3h).

Atmospheric-Induced Corrosion

Fig. 3 (a) shows the 2205 sample with dried salt deposits and local corrosion attack (circle) after AIC exposure. Both, the 2205 and 2507 as-received grades showed preferential attack on ferrite and along ferrite/austenite interfaces, shown on grade 2205 in Fig. 3 (b-d). Most of the observed attack was superficial, summarised in Fig. 3 (c-d). EDX analysis of the box highlighted in Fig. 3 (d) indicated the presence of an austenitic grain facet, possibly exposed due to corrosion attack. Ferrite has generally higher chromium and molybdenum contents, and it is surprising that this phase seemed to be more prone to corrosion attack. Similar observations have also been reported in other investigations [4].

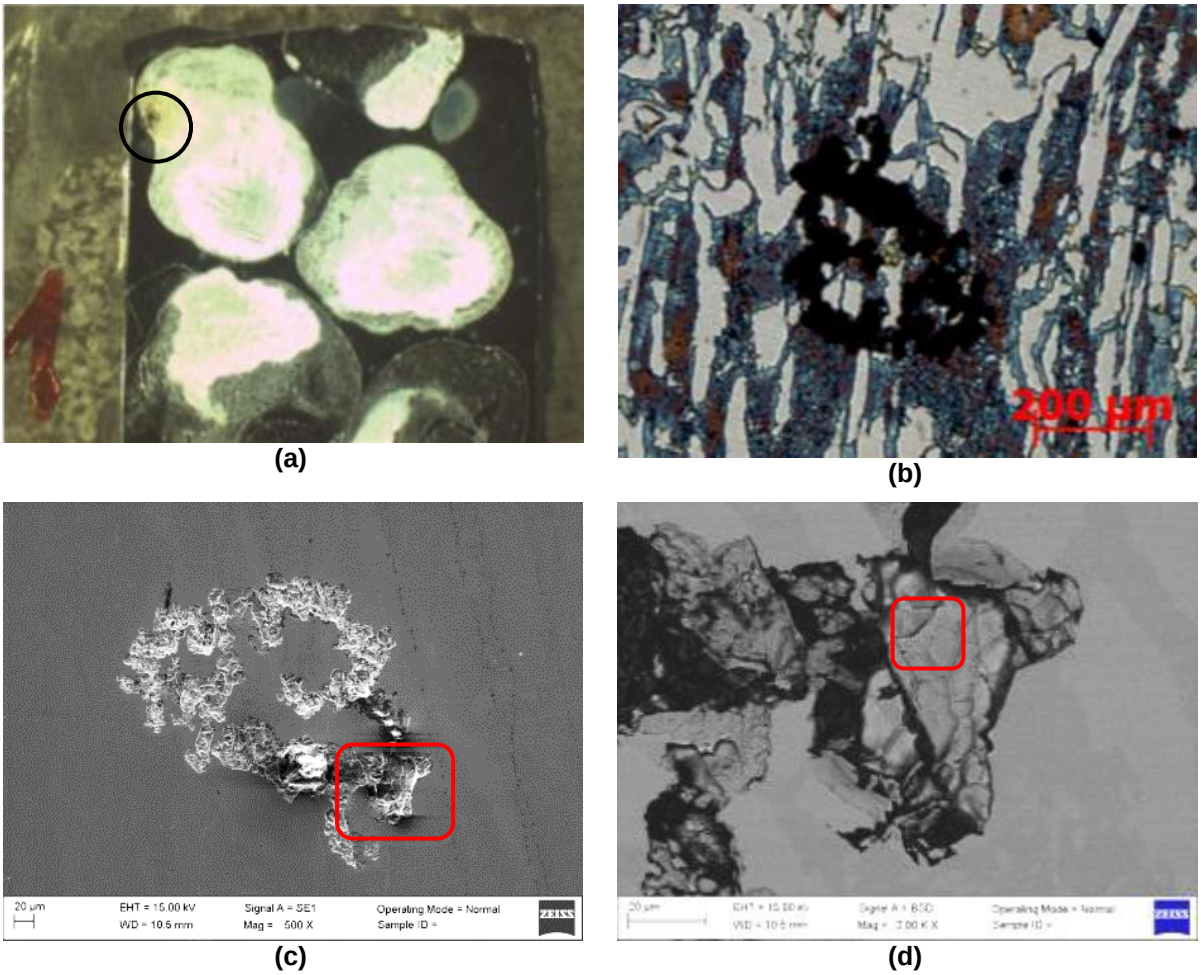

(a) **(b)** **(c)** **(d)**

Fig. 3: (a) Image of dried $MgCl_2$ salt droplets on the as-received 2205 sample; (b) optical image of the corrosion attack after removal of the dried deposit (KOH etched to colour ferrite), (c) SEM image of a corroded region; (d) higher magnification SEM/BSE image of the box shown in (c).

The 750°C heat-treated grade 2205 sample showed preferential attack along ferritic regions, extending along austenite/ferrite interfaces with some attack on austenite, shown in Fig. 4 (a-b). Selective corrosion possibly initiated at α/γ-phase boundaries, and proceeded into the ferrite. Corrosion attack may have also been promoted by the presence of secondary phases (Fig. 1 b), or their element depleted zones, but this could not be confirmed in this study.

Interestingly, the 750°C heat-treated grade 2507 sample showed dissolution of primary (γ) and secondary austenite (γ‘), with only some attack on sigma phase, shown in Fig. 4 (c-d). The attack under the deposit was so severe that large regions

in the primary austenite and the secondary austenite (prior ferrite) were simply corroded away. However, no ferrite could be observed via EDX measurements in the region investigated. It has been reported that γ' formed via the eutectoid transformation contains less Cr and Mo, hence this phase may therefore have lower corrosion resistance than the primary austenite [10]. However, mainly the high-chromium/molybdenum containing χ-phase remained in the microstructure (Fig. 4 c-d), with some remaining σ -phase in prior ferrite grains (Fig. 4 d).

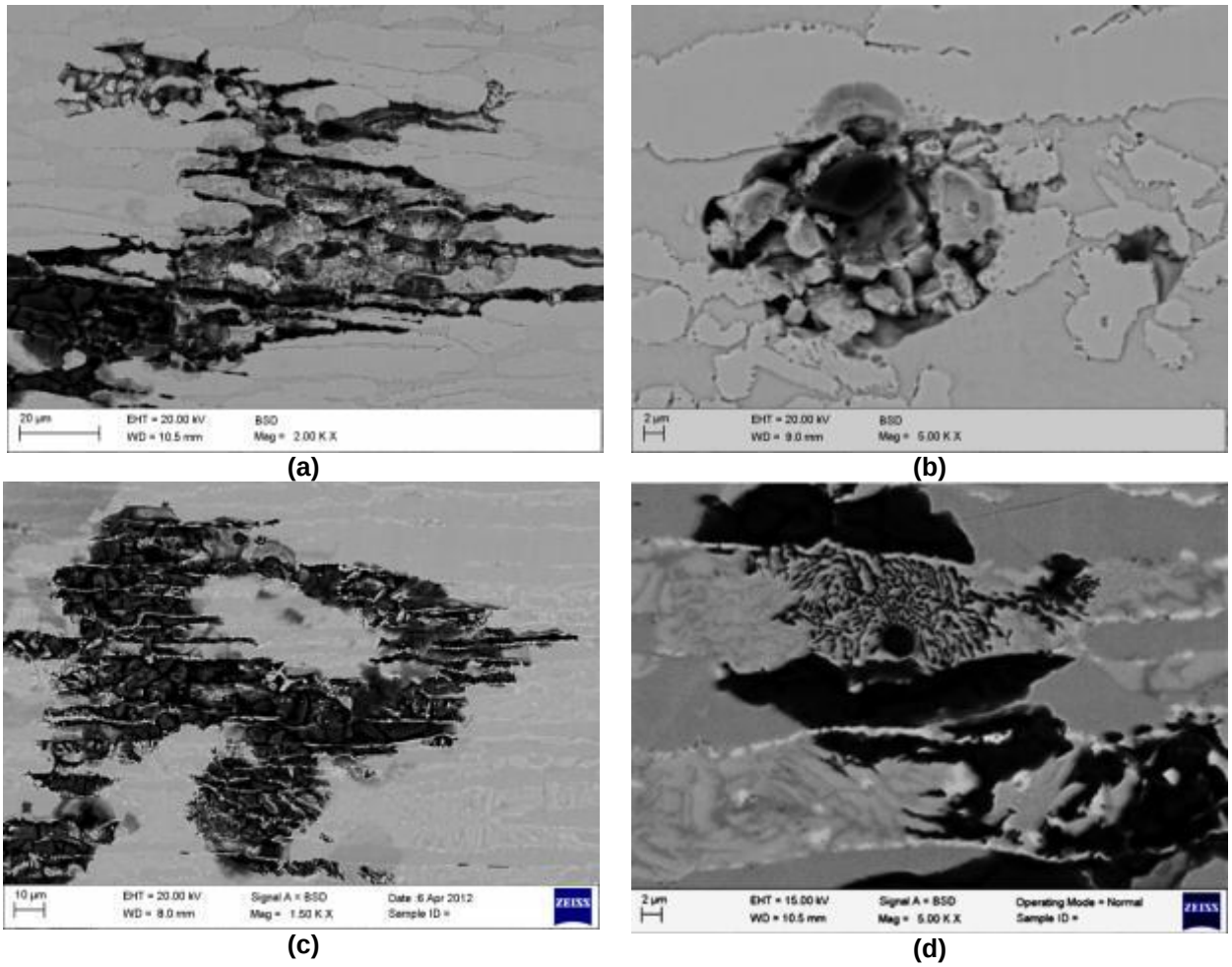

Fig. 4: (a-b) Selective corrosion attack of heat-treated grade 2205, (c-d) and selectively corroded regions of heat-treated grade 2507.

SKPFM and MFM of Grade 2205

Fig. 5 shows images of the surface topography, local Volta potential differences (Δψ) and magnetic frequency differences (ΔMf) of the as-received grade 2205 sample. The peak surface roughness measured was ca. 15 nm, shown in Fig. 5 (a-b), and the (ΔMf) values in Fig. 5 (e-f) allow the phases in the microstructure to be distinguished for the identification of ferrite and austenite. A real-time plane-fit was applied to the Δψ and ΔMf values, which removed the Z offset from the entire image.

Potential contrast measured by SKPFM is limited, as SKPFM is prone to stray capacitance as a result of interactions between the specimen and the cantilever, which in the case of alloy systems can serve to reduce the measured potential difference [6]. If a correlation exists between surface potentials measured in air and the resulting corrosion behaviour, Δψ can only be interpreted as an indicator of the

relative nobility of the phases present [15]. However, it should be noted that Δψ values reported in this work are of opposite sign to corrosion potentials, a result of the electronic configuration of the instrument; hence a higher Δψ value indicates in our work a net anode.

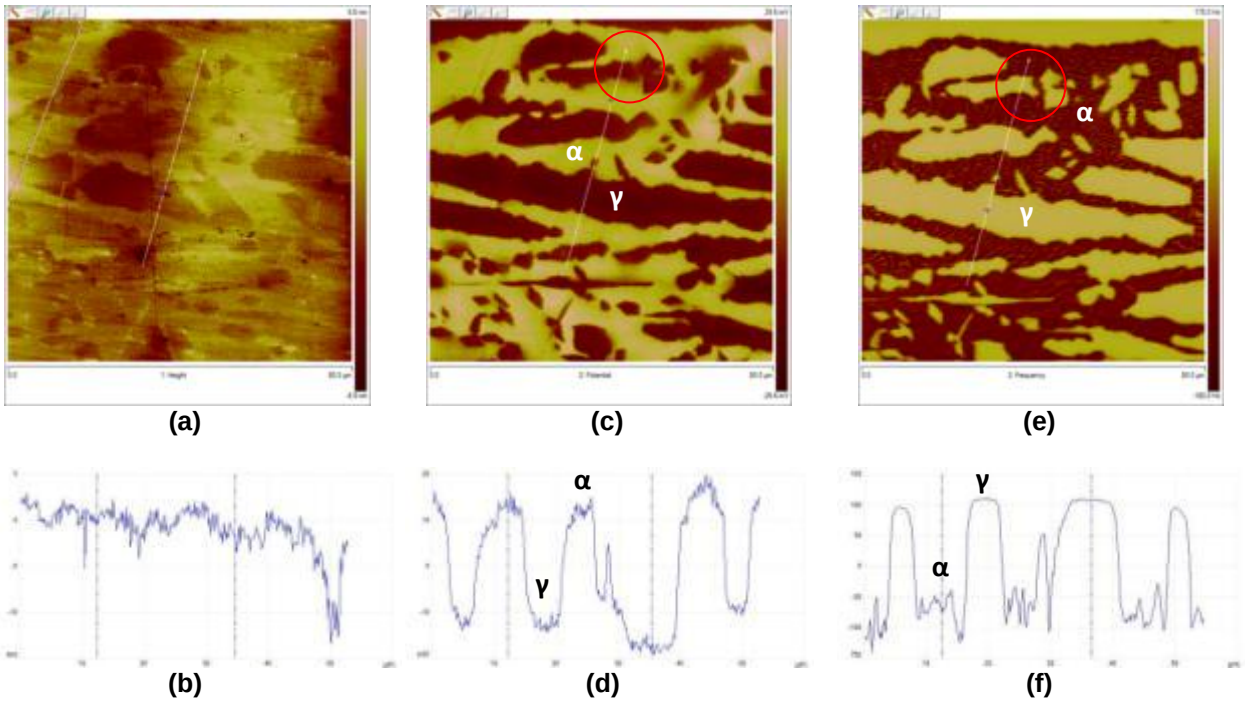

Fig. 5: Grade 2205 as-received (a-b) surface topography map and profiles; (c-d) Surface potential differences (Δψ) map and profiles; (e-f) MFM (Δ$M\ƒ$) map and profiles

In Fig. 5 (c-d) the relative Δψ values for the ferritic regions are higher than the austenitic regions, and hence ferrite would be expected to function as a net anode. These observations are supported by atmospheric-induced corrosion results on the as-received materials, in which ferrite and the ferrite/austenite boundary were attacked, with the primary austenite behaving as the net cathode (Fig. 3). The corresponding MFM images in Fig. 5 (e-f) allow the phases present in the microstructure to be distinguished, with the dark regions representing the ferrite. Sathirachinda et al. [16] have shown similar results for solution annealed grade 2205, where ferrite was the net anode, and Femenia i Nobell [17] and Guo [18] interpreted their results on grade 2205 for austenite to behave as net cathodes.

In Fig. 5 (c) and Fig. 5 (e) the red circles also show that ferrite in close proximity to austenite seems to have a low Δψ value, i.e. the small ferrite bridge in Fig 5 (e) seems to be cathodic in comparison to the main ferritic areas. This observation is currently under investigation to rule out the presence of artefacts, for example due to the 3D nature of the microstructure.

Fig. 6 shows the Δψ and Δ$M\ƒ$ values of heat-treated grade 2205. The surface potential image seems more diffuse around the edges of the individual phase boundaries (Fig. 6 c), which is also reflected in the MFM image (Fig. 6 e). Interestingly, along the austenite/ferrite phase boundary, gradual transitions in Δ$M\ƒ$ can be seen, in comparison to a steep transition in the as-received microstructure. It may be inferred that once significant elemental depletion occurred, for example due to the precipitation of secondary phase, changes in Δψ and Δ$M\ƒ$ may take place. Second phase precipitates were only observed in heat-treated microstructures,

whereas in the as-received microstructure no σ and χ phase was seen. Sathirachinda et al. [16], for example, have shown for long-term heat-treated grade 2205 that γ can become more anodic compared to the sigma phase [15].

Distinctive ΔMf variations within the ferrite are possibly related to changes in the magnetic domains, indicating regions with locally different magnetic behaviour (Fig. 6 f). Ferrite has higher Δψ values and is therefore expected to behave as a net anode, which was also observed in our AIC tests of heat-treated grade 2205. The Δψ values measured by SKPFM in air seem to correlate with the atmospheric corrosion behaviour of the as-received and heat-treated grade 2205. Information obtained in this study will be used to set-up and characterise microstructure for in-situ AISCC testing at temperatures more relevant to ambient exposure conditions, i.e. at temperatures below 50°C.

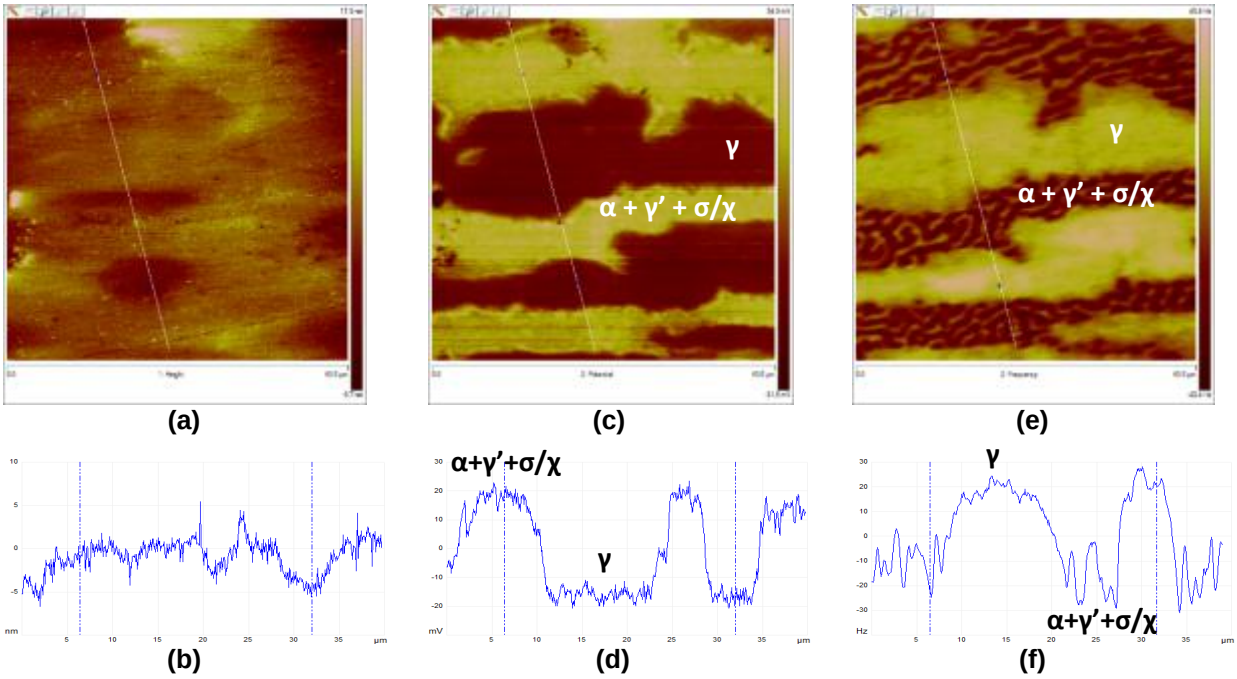

Fig. 6: Heat-treated grade 2205 (750°C/3h) (a-b) surface topography map and profile; (c-d) Δψ map and profiles; (e-f) ΔMf map and profiles.

Conclusions

- In as-received grade 2205 and 2507, ferrite was more prone to corrosion than austenite. SKPFM measurements supported this observation, and indicated that ferrite may behave as net anode.

- After heat treatment at 750°C for 3 hrs, ferrite, austenite, chi/sigma, and possibly secondary austenite were present in the 2507 and far less in the 2205 microstructures. No ferrite was found in the regions characterised in heat-treated 2507, with prior ferrite regions mainly containing secondary austenite, chi, and sigma phase precipitates.

- After heat treatment at 750°C, both materials were more prone to corrosion, with only the high Cr/Mo-containing phases remaining at some locations.

- Ferrite was selectively attacked in heat-treated grade 2205, whereas primary and secondary austenite was attacked in heat-treated grade 2507.

Acknowledgement

The authors acknowledge helpful discussions with Dr. J. Walton and Dr. A. B. Cook, Corrosion and Protection Centre, The University of Manchester. The authors are grateful for the Nuclear Decommissioning Authority (NDA) for their financial support through the research grant NDA/EPSRC (EP/I036397/1).

References

[1] Iris Alvarez-Armas: Duplex Stainless Steels: Brief History and Some Recent Alloys; Recent Patents on Mechanical Engineering, 1, (2008), 51-57

[2] Nuclear Decommissioning Authority, Geological Disposal: Package Evolution Status, NDA Report NDA/RWMD/031, (2010)

[3] F. King: Corrosion Resistance of Austenitic and Duplex Stainless Steels in Environments Related to UK Geological Disposal, Document number: QRS-1384C-R1, Version 1.2, Quintessa Limited, (2009)

[4] T. Prosek, A. Iversen, C. Taxén, D. Thierry: Low-Temperature Stress Corrosion Cracking of Stainless Steels in the Atmosphere in the Presence of Chloride Deposits, Corrosion, Vol. 65, No. 2 (2009)

[5] G. Hinds, A. Thurnbull.: Threshold Temperature for Stress Corrosion Cracking of Duplex Stainless Steel Under Evaporative Seawater Conditions, Corrosion Science, 64, No.2, (2008)

[6] A. B. Cook, Z. Barrett, S. B. Lyon, H. N. McMurray, J. Walton, G. Williams: Calibration of the scanning Kelvin probe force microscope under controlled environmental conditions, Electrochmica Acta, 66, (2012), 100–105

[7] M. Rohwerder, F. Turcu: High-resolution Kelvin probe microscopy in corrosion science: Scanning Kelvin probe force microscopy (SKPFM) versus classical scanning Kelvin probe (SKP), Electrochimica Acta, 53, (2007), 290-299

[8] N. Sathirachinda, R. Petterson, S. Wessman, J. Pan: Study of nobility of chromium nitrides in isothermally aged duplex stainless steels by using SKPFM and SEM/EDS, Corrosion Science 52, (2010), 179-186

[9] S. Takaya, T. Suzuki, T. Uchimoto, K. Miya: Magnetic force microscopy observation of sensitized Inconel 600, Journal of Applied Physics, 91, 7011 (2002)

[10] S. Topolska, J. Labanowski: Effect of microstructure on impact toughness of duplex and super duplex stainless steels, Journal of Achievements in Materials and Manufacturing Engineering. 36, 2, (2009)

[11] S. P. Trasatti, S. Cristini, B. Sacchi, E. Guerrini: Detection of Sigma Phase in 22% Cr Duplex Stainless Steel by Electrochemical Methods, Russian Journal of Electrochemistry, 46, No. 10 (2010), 1094-1100

[12] M. E. Arıkan, R. Arıkan, M. Doruk: Determination of Susceptibility to Intergranular Corrosion of UNS 31803 Type Duplex Stainless Steel by Electrochemical Reactivation Method, International Journal of Corrosion, Vol. 2012, Article ID 651829, (2012)

[13] Y.-J. Kim: Microstructural Evolution of Secondary Phases in the Cast Duplex Stainless Steels CD3MN and CD3MWCuN, The Minerals, Metals & Materials Society and ASM International, 38A, (2008)

[14] J. M. Padal, S. S. M. Tavares, M. P. C. Fonseca, J. A. Souza, L. M. Vieira, H. F. G. de Abreu: Deleterious Phases Precipitation on Superduplex Stainless Steel UNS S32750: Characterization by Light Optical and Scanning Electron Microscopy, Materials Research, 13, 3, (2010), 401-407

[15] N. Sathirachinda, R. Pettersson, S. Wessman, J. Pan: Study of nobility of chromium nitrides in isothermally aged duplex stainless steels by using SKPFM and SEM/EDS, Corrosion Science, 52, (2010), 179-186

[16] N. Sathirachinda, R. Pettersson, J. Pan: Depletion effects at phase boundaries in 2205 duplex stainless steel characterized with SKPFM and TEM/EDS, Corrosion Science, 51, (2009), 1850-1860

[17] Marc Femenia i Nobell: Doctoral Thesis: Corrosion Behavior of Duplex Stainless Steels in Acidic-Chloride Solutions Studied with Micrometer Resolution, Royal Institute of Technology, Sweden, 2003

[18] M. Li, L.Q. Guo, L.J. Qiao, Y. Bai: The mechanism of hydrogen-induced pitting corrosion in duplex stainless steel studied by SKPFM, Corrosion Science, Vol. 60, (2012)